Toward Three-Dimensional Quantum State-Resolved Collision Dynamics at the Gas−Liquid Interface: Theoretical Investigation of Incident Angle†

Bradford G. Perkins, Jr. and David J. Nesbitt*

JILA, University of Colorado and National Institute of Standards and Technology, and Department of Chemistry and Biochemistry, University of Colorado, Boulder, Colorado 80309-0440

Received: December 22, 2008; Revised Manuscript Received: February 24, 2009

Quantum state-resolved energy transfer dynamics at the gas−liquid interface are explored through a comparison of classical molecular dynamics (MD) simulations and previously reported experimental studies (Perkins, B. G.; et al. *J. Phys. Chem. A* **2008**, *112*, 9234). Theoretically, large scale MD trajectory calculations have been performed for collisions of CO_2 with a model fluorinated self-assembled monolayer surface (F-SAMs), based on an explicit atom-atom interaction potential obtained from earlier theoretical studies (Martínez-Núñez, E.; et al. *J. Phys. Chem. C* **2007**, *111*, 354). Initial conditions for the simulations match those in the experimental studies where high-energy jet-cooled CO_2 molecules (E_{inc} = 10.6(8) kcal/mol, $<E_{rot}> \approx 10$ cm^{-1}) are scattered from a 300 K perfluorinated liquid surface (PFPE) from a range of incident angles (θ_{inc} = 0−60°). Nascent CO_2 rotational distributions prove to be remarkably well characterized by a simple two-temperature trapping-desorption (TD) and impulsive scattering (IS) model with nearly quantitative agreement between experimental and theoretical column integrated densities. Furthermore, three-dimensional (3D) quantum state resolved flux maps for glancing incident angles ($\theta_{inc} \approx 60°$) reveal broad, lobular distributions peaking strongly in the forward subspecular direction as $\cos^n(\theta_{scat} - \theta')$ with $n \approx 5.6(1.2)$ and $\theta' \approx 49(2)°$.

I. Introduction

Collision dynamics at the gas−liquid interface are important in a wide variety of chemical processes with final angular and quantum state distributions reflecting a variety of paths that include direct scattering, surface trapping, and long-time solvation.[1−3] Experimental access to this important arena has relied heavily on elegant experimental molecular beam techniques developed to investigate single crystal, gas−solid interfaces,[4] which indeed have yielded enormously detailed and valuable microscopic insights into physical phenomena such as catalysis, physisorption, and chemisorption.[5−12] Recent molecular beams studies have attempted to provide similarly detailed insights into the surface of liquids,[13−28] and in particular to characterize the potential role of transient structure, dynamical motion, and other differences between gas−solid and gas−liquid interfaces.

A critically important element in this broader exploratory effort has been rigorous theoretical investigation,[29−36] based on obtaining reliable interaction potentials between a particular gas and liquid system, and then performing molecular dynamics (MD) simulations of the collisional events. Time after time, this ongoing comparison between experiment and theory has helped uncover the most important details for our understanding, where one technique compliments the other in elucidating key chemical and physical processes at the interface.[29,32,36−43] In an effort to harness this symbiotic power between experiment and theory, the focus of our current study follows from the work of many others in the chemical physics community, [29−47] where we compare previous experimental studies of CO_2 + perfluorinated liquids (PFPE) with detailed theoretical MD simulations of CO_2 + fluorinated self-assembled monolayers (F-SAMs). In this comparison, we utilize results from theoretical trajectories to extract final scattering distributions and time-dependent surface structural metrics to help understand energy transfer dynamics at the gas−liquid interface, and in particular what might distinguish such dynamics from those at a gas–solid surface.

The current paradigm of gas−liquid collision dynamics is illustrated in Figure 1, where an incident gas molecule scatters inelastically from the surface through one of two characteristic pathways, historically referred to as trapping-desorption (TD) and impulsive scattering (IS).[1,13−22] The TD component reflects equilibrium with the surface through a series of thermalizing interactions, followed by eventual desorption. On the basis of previous CO_2 + perfluorinated liquid scattering studies that reveal unity sticking probabilities for low incident energies ($E_{inc} < 5kT_S$, where T_S is surface temperature),[20,32,36,48] molecules in the TD channel desorb from the surface with internal state and translational distributions well-characterized by surface temperature Maxwell−Boltzmann probabilities. In contrast, the IS channel reflects events with more abbreviated collisional interactions with the surface, where the scattering distributions often span a higher range of final energies. Microscopic branching into one channel over the other has been investigated by several groups, where experimental detection schemes include time-of-flight mass spectrometry (TOFMS),[13−15] laser-induced fluorescence (LIF),[23−25,49,50] and direct infrared absorption.[16−22] For example, the Minton group has measured in-plane detection of O, OH, and H_2O for inelastic and reactive scattering of O(^{3}P) + squalane ($C_{30}H_{62}$), where scattered fluxes were detected by a rotatable mass spectrometer.[26−28,51−53] With E_{inc} = 11.2 kcal/mol at $\theta_{inc} = 60°$, inelastic scattering results for the O(^{3}P) show two distinct channels when binned by final velocities. Flux from the TD component is well-characterized by a $\cos(\theta_{scat})$ distribution, whereas molecules scattering via the IS channel follow $\cos^n(\theta_{scat} - \theta')$ with $n \approx 6$ and $\theta' \approx 42°$. The lobular final distributions reflect substantial variation in the local collision

† Part of the "George C. Schatz Festschrift".

* To whom correspondence should be addressed. E-mail: djn@jila.colorado.edu.

10.1021/jp811322y CCC: $40.75
Published on Web 03/31/2009

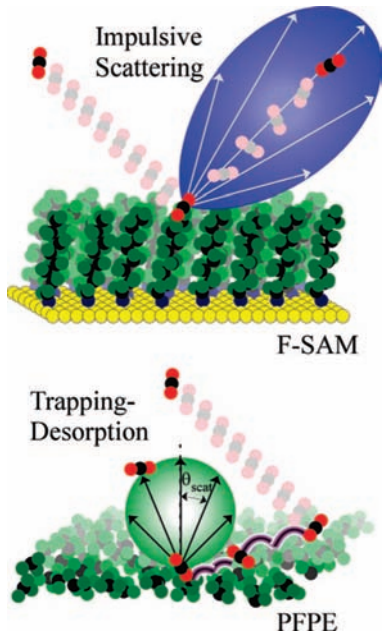

Figure 1. Experimental and theoretical studies probe interfacial dynamics of perfluorinated liquid surfaces. CO_2 molecules scatter from the surface through two channels, historically described as impulsive scattering (IS) and trapping-desorption (TD). Chemical dynamics simulations compliment quantum-state resolved experiments to reveal a molecular-level perspective of the interfacial dynamics.

geometries between the gas and liquid. Studies to include out-of-plane scattering have been limited, however, due to the additional experimental complexity required.[52] Indeed, full three-dimensional (3D) reconstruction of the state-resolved scattering distributions would provide important insight into the fundamental nature of the gas−liquid interaction and yet has thus far remained elusive.

Recent efforts in our laboratory have focused on developing methods for extracting such experimental 3D distributions from CO_2-liquid PFPE scattering events, where both translational distributions and internal state populations of the scattered flux have been measured with direct absorption high resolution spectroscopy.[16,19,20,22] Under a broad range of incident conditions, the TD and IS populations are both well-characterized by temperatures, where $T_{rot}(TD) \approx T_S \approx 298$ K and $T_{rot}(IS) > T_S$. While a T_S distribution is expected for the TD population, the hot IS temperature suggests that an impulsive interaction at the gas−liquid interface includes a distribution of single and multiple collisions with the surface.[20] On the basis of the results of our initial experiments,[16,17,19,20,22] further studies evolved to systematically uncover TD and IS dynamics for $\theta_{inc} = 0$, 30, 45, and 60° over a range of final scattering angles that include $\theta_{scat} = -60$ to $+60°$.[18] Within the experimental configuration illustrated in Figure 2a, high resolution absorption profiles were measured for a given pair of incident and final angles, where each Doppler profile reflects data on both in-plane ($|\nu - \nu_0| \approx 0$) and out-of-plane ($|\nu - \nu_0| > 0$) scattering trajectories. From these absorption profiles, we calculated internal state populations, and then fit the distribution to a two-temperature rotational state model to separate the TD from IS fraction in the scattered flux. By assuming the TD flux desorbs as $\cos(\theta_{scat})$, results from this study show that the IS component is surprisingly well-characterized by $\cos^n(\theta_{scat})$ with $n \approx 1$ for normal incidence. As the incident angle shifts away from 0°, CO_2 preferentially scatters in the forward direction with a larger fraction of its initial energy, which is partitioned into rotation and translation, but not vibration of the CO_2.

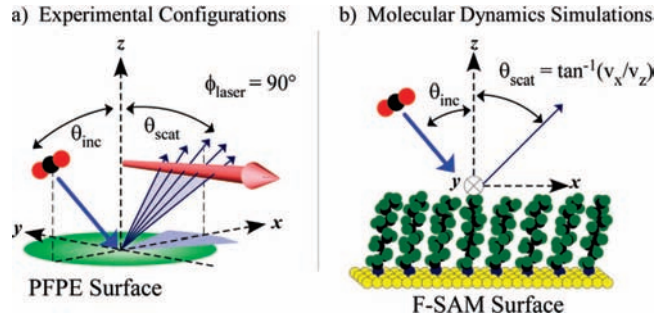

Figure 2. Detailed illustration of experimental and simulation scattering geometries. (a) Final internal state populations for CO_2 + PFPE are determined from a systematic incident molecular beam, liquid surface, and laser detection scheme to study the full 3D scattering distributions. High resolution absorption profiles reflect in-plane ($|\nu - \nu_0| \approx 0$) and out-of-plane ($|\nu - \nu_0| > 0$) scattering for a given pair of incident and final scattering angles. (b) MD simulations provide a theoretical description of the gas−liquid interface. The coordinate systems are illustrated in each figure.

TABLE 1: Bulk and Surface Properties of PFPE Liquid and F-SAMs

	PFPE[a]	F-SAM[b]
chemical composition	F−[CF(CF_3)CF_2O]$_{14}$−CF_2CF_3	Au−S(CF_2)$_7CF_3$
density	1.87 g/cm^3	1.93 g/cm^3
vapor pressure	7×10^{-7} Torr	$<5 \times 10^{-10}$ Torr
thermal expansion	8.3×10^{-4} K^{-1}	1.0×10^{-3} K^{-1}
surface tension	17 dyne/cm	10−15 dyne/cm
surface roughness	≈7 Å[c]	≈4 Å [d]

[a] Krytox 1506 polymer, Dupont. See ref 54 for further details. [b] Properties reported in refs 16, 55, 56, 59, and 60. [c] Root mean square (rms) width of the surface region (δ) is approximately $[(kT_{liq}/2\pi\gamma) \times \ln(2\pi L_c/d)]^{1/2}$ where γ is the surface tension, $L_c = (\gamma/g\,\rho)^{1/2}$, and d is roughly the length of a PFPE molecule (≈100 Å). [d] Determined from combination of AFM studies[59,60] and 100 ps trajectory simulations.[16]

An alternative and complimentary approach toward uncovering the 3D scattering distributions for CO_2 + PFPE involves theoretical MD studies of CO_2 + F-SAM surface.[32,36] On the basis of the similarity of properties listed in Table 1,[16,54−56] MD trajectories with CO_2 + F-SAMs have been calculated to compare and contrast early experimental studies of CO_2 + PFPE in our laboratory. Studies have included varying incident energy[32,36] and surface temperature,[16] where the theoretical results have quantitatively reproduced the experimental measurements. The high quality of agreement between simulations and gas−liquid scattering results suggests the collision dynamics with F-SAM and PFPE to be remarkably similar, at least as sampled by our experiments. With this in mind, our current study extends the comparison between theory and experiment to incident trajectories at $\theta_{inc} = 30$, 45, and 60°. Previous experimental studies of specular scattering[19] have shown that the TD fraction (α) decreases as θ_{inc} increases, which implies a qualitative shift in the nature of gas−liquid interactions at the interface. The decrease in α may reflect a change in the number of collisions, characteristic time spent on the surface, or energy transferred per surface interaction. The dynamics of each of these phenomena are determined by the motion of the liquid surface on the time scale of the collision, with respect to both rotation and translation of CO_2. Motion of the liquid surface on these time scales is dominated by low frequency vibrations, which consist of torsional wags, bends, and collective surface vibrations within capillary waves. A detailed comparison of the PFPE experimental results and F-SAM simulations provides the

opportunity to characterize the similarities and differences between two types of liquid interfaces, where specifically, the dynamical motion of the surface directly influences the scattering. Such a characterization helps illustrate important differences between gas−liquid and gas−solid behavior, where the frequency and amplitude of various surface modes can influence the scattering dynamics.

The remaining sections of this study are outlined as followed. Section II contains abbreviated details of the CO_2 + PFPE experiment, as well as a description of the important components of the MD calculations. The two-temperature model is outlined in Section III. In addition, results from the theoretical simulations are presented where the analysis involves a direct comparison with the experimental studies. Section IV presents final angular distributions based on the MD simulations. Concluding remarks are made in Section V.

II. Methods

Details of the experiment may be found in previous studies;[16−20,22] therefore, we present only a brief overview to illustrate the important components of the measurements so that the comparison with the theoretical results is clear. The experiment consists of a supersonic molecular beam of CO_2 (E_{inc} = 10.6(8) kcal/mol; $T_{rot} \approx 15$ K) that impinges upon a clean liquid surface in vacuum, with ground (00^00) and bend-excited (01^10) quantum state rotational populations in the incident and scattered flux probed by high resolution direct IR laser absorption.[57] The cartoon illustration in Figure 2a depicts the general scheme for the range of experimental configurations. Molecules impinge upon the surface with a fixed incident angle (θ_{inc}) between the molecular beam expansion axis and surface normal (z-axis). The studies sample incident angles of 0, 30, 45, and 60°, with molecules approaching in the $x-z$ plane. Results in the present study reflect laser beam propagation parallel to the y-axis (i.e., $\varphi_{laser} = 90°$) and therefore nominally perpendicular to the scattering plane. The final probe geometry is characterized most simply by θ_{scat}, the angle between (i) the surface normal, (ii) the impact point on the surface, and (iii) the point at which the laser beam passes through the $x-z$ plane. High resolution Doppler profiles in this geometry provide additional information on both out-of-plane as well as in-plane collision dynamics. Specifically, absorbance signals near the rest frequency ($\nu - \nu_0 \approx 0$) reflect in-plane scattering, while signals with large frequency detuning ($|\nu - \nu_0| > 0$) reflect a significant out-of-plane scattering component.

In terms of theoretical calculations, previous chemical dynamics simulations have successfully incorporated models of gas-surface interactions to quantitatively reproduce experimental studies. In our study, we use a published fluorinated hydrocarbon potential for the thiol molecules in an explicit atom model,[58] where the F-SAM surface is assembled from 48 alkylthiolate chains of $CF_3(CF_2)_7S$ chemisorbed to a layer of Au(111) atoms.[32] Each chain is anchored to the Au surface with a harmonic stretch potential to simulate adsorption of a monolayer.[32] Other molecular bonds (S−C, C−C, and C−F) in the fluorinated thiol chains are similarly constructed as harmonic stretches with characteristic force constants and equilibrium distances. Additional nonbonding terms including bending interactions, torsional potentials, and van der Waals forces are calculated from the parameters listed in ref 58. MD simulations of a 300 K surface with these values accurately capture experimentally determined properties such as a ≈12° tilt angle, density of 1.93 g/cm^3, and hexagonal close-packed structure.[32,59,60] In addition to a suitable potential model for the fluid-like F-SAM, an accurate CO_2-surface interaction potential is also required to predict forces throughout a trajectory. For this we take advantage of ab initio potential data for $CO_2 + CF_4$ calculated by Martínez-Núñez et al. for which the C−C, C−F, O−C, and O−F interactions have already been characterized. Details of the fits and a list of the parameters may be found in ref 32. On the basis of these results, the gas-surface interaction is given by a sum of two-body potentials composed of long-range attraction ($-C/r^n$) and short-range exponential repulsion between individual atoms in the CO_2 projectile and F-SAM surface.

MD simulations with VENUS05 software[61] combine the model F-SAM surface and CO_2-surface potentials to provide a detailed description of a scattering system with liquidlike characteristics. Similar to the experimental geometry, we define coordinates in Figure 2b for the CO_2 + F-SAM simulations, where x and y define the surface plane and z is the surface normal. Incident CO_2 molecules are directed toward the surface in the positive x direction in the $x-z$ plane, with initial conditions chosen to match the experimental studies. Specifically, the incident energy for the CO_2 is fixed at 10.6 kcal/mol with rotational states sampled from a 15 K distribution. The studies include incident polar angles of $\theta_{inc} = 0$, 30, 45, and 60°, where the incident azimuthal angle (φ_{inc}) is randomly sampled from $0-2\pi$ to average over any residual directionality and tilt in the F-SAM surface. An initial 2 ps simulation prior to releasing the projectile ensures that the F-SAM structure reflects an equilibrium distribution, with average kinetic energies adjusted to correspond to a 300 K surface. Before the trajectory begins, the CO_2 is aimed toward randomly selected points within the central unit cell from a height of 25 Å above the F-SAM surface. Position and momenta for each atom are then integrated (0.3 fs step size) using the Adams−Moulton algorithm with periodic boundary conditions applied throughout the calculation to increase interaction area for CO_2 as it collides with the F-SAM surface. Trajectories are stopped when either (i) the height of the returning CO_2 exceeds its starting position with a positive v_z, or (ii) the integration time exceeds 150 ps, at which point final translational, rotational, and angular distributions for the scattered molecule are determined. For the small 1−2% fraction of trajectories that survive past 150 ps, the CO_2 molecules are assumed to have thermally equilibrated with the surface, which allows us to simply sample final J-states and flux-weighted velocities from a 300 K distribution.

III. Results

A. Two-Temperature Boltzmann Model. Internal state populations have been experimentally measured and reported in ref 18 for scattered CO_2 + PFPE as a function of initial and final scattering angles.[18] The experimental configurations have been systematically varied to detect scattered CO_2 molecules over nearly 2π steradian solid angle. Populations at each configuration show non-Boltzmann distributions that have been analyzed with a two-temperature model. To help illustrate the parameters of the model and provide a basis for later comparison with theoretical results, sample Doppler-broadened profiles for scattered CO_2 (00^00) are plotted in Figure 3a for a configuration of $\theta_{inc} = 45°$ and $\theta_{scat} = 0°$. The individual Doppler profiles reflect the velocity projection (i.e., coupled translational and angular distributions) along the laser probe axis, while the progression of J-states within the vibrational manifold characterizes the extent of rotational excitation for the particular experimental geometry. Our primary analysis efforts to this point have focused on column-integrated v,J-state densities, ($A_{v,J}$), generated from these Doppler profiles by integration over all detuning frequencies. The two-temperature Boltzmann analysis

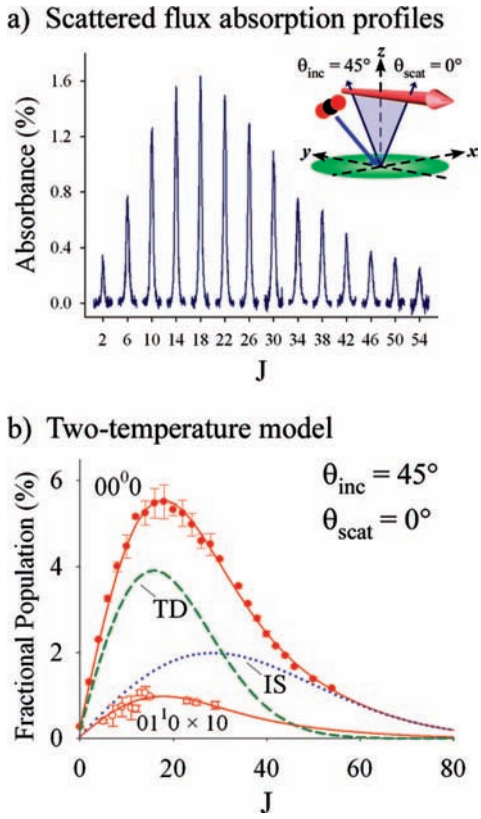

Figure 3. Sample experimental data for $E_{inc} = 10.6(8)$ kcal/mol, $\theta_{inc} = 45°$ and $\theta_{scat} = 0°$. (a) High resolution absorption profiles reflect quantum-state populations within the ground vibrational manifold (00^00). States with $J > 54$ are not accessible with the current diode laser. b) Populations are characterized by a two-temperature model, where $T_{rot}(TD) = 298$ K, $T_{rot}(IS) = 940(80)$ K, and the TD fraction (α) is 0.53(2).

of $A_{v,J}$ extracts subpopulations and provides important information on energy transfer between the incident gas and liquid surface.[22]

The model assumes that the measured populations at a given experimental configuration are composed of two components, TD and IS, where the rotational distribution for each is well characterized by a temperature, T_{rot}(TD/IS). The microscopic branching between IS and TD channels is defined by the TD fraction (α), which reflects a column density-based characterization of the sticking probability for a given scattering angle. Additionally, our model fits J-state populations in each vibrational state to the same TD and IS rotational temperatures, where the fractional difference between 00^00 and 01^10 state populations characterizes the vibrational temperature, T_{vib}. On the basis of these assumptions, the column densities are fit explicitly to the function

$$\frac{A_{v,J}}{S_{v,J}} = N[\alpha P_J(\mathrm{TD}) + (1 - \alpha)P_J(\mathrm{IS})]P_v \qquad (1)$$

where $S_{v,J}$ is the appropriate Hönl-London line strength factor, N is an overall scaling factor, and P_J(TD), P_J(IS), and P_v are normalized Boltzmann factors for rotation and vibration, respectively.[18] We assume that the TD population is thermally equilibrated with the surface, which allows us to fix $T_{rot}(TD) \approx T_S = 298$ K and break parameter correlations in the nonlinear least-squares algorithm. Such an assumption is supported by detailed balance considerations for incident energy dependence of the sticking probability,[20,48] as further confirmed by detailed scattering studies as a function of liquid surface temperature.[16] The data for each $\theta_{inc}/\theta_{scat}$ pair are fit to extract T_{rot}(IS), T_{vib}, and α, at which point the individual quantum-state populations are normalized from the extracted fit parameters to generate fractional populations. To illustrate this process, populations from sample absorption profiles in Figure 3a are plotted in Figure 3b along with the total fit (solid line) broken down into individual TD (dashed line) and IS (dotted line) components. For $E_{inc} = 10.6(8)$ kcal/mol and $\theta_{inc} = 45°$ experimental conditions, probing at $\theta_{scat} = 0°$ yields (i) nearly equal microscopic branching into TD versus IS channels [$\alpha = 0.53(2)$], (ii) quite hot IS rotational distributions [$T_{rot}(IS) = 940(80)$K], and yet (iii) vibrational bend populations [$T_{vib} = 238(8)$ K] even colder than the actual 298 K surface temperature. Summary data in Table 2 in ref 18 reveal clear trends as a function of final scattering angle; the sticking coefficient α decreases dramatically for forward vs backward directions. However, in each case, molecules in the IS channel exit with considerable rotational energy ($T_{rot}(IS) \gg T_S$), yet negligible vibrational excitation ($T_{vib} < T_S$) in the gas-surface interaction.

B. Theoretical Results: Angle-Resolved Scattering and Flux-to-Density Transformations. In contrast with experimental measurements of column integration densities at a fixed scattering angle θ_{scat}, the MD simulations provide actual flux distributions for all trajectories within the entire 3D scattering space. To break this further down into a rotational state distribution, the quantum state (J) is determined from the classical angular momentum by $j = [J(J + 1)]^{1/2}\hbar$ with final J-states binned in a histogram that is normalized to the total number of trajectories. A sample rotational state distribution, P_J(flux), is plotted in Figure 4a for $\theta_{inc} = 45°$. From the shape of the histogram, we again notice that the rotational states appear to be best described by more than one temperature. On the basis of related distributions in previous CO_2+F-SAM simulations,[16,32,36] we fit P_J(flux) with a two-temperature model similar to eq 1, where the explicit functional form for flux analysis is

$$P_J(\mathrm{flux}) = \alpha_f P_J(\mathrm{TD}) + (1 - \alpha_f)P_J(\mathrm{IS}) \qquad (2)$$

P_J(TD) and P_J(IS) are identical to the terms defined previously. The flux-weighted TD fraction (α_f) now reflects the total fraction of incident molecules that stick to the surface and parallels the conventional definition of sticking coefficients. Because of theoretical inclusion of higher rotational states than experimentally accessible with our current diode laser, parameter correlation issues are now much improved; floating all three parameters, we find that $T_{rot}(TD) = 268(15)$ K, $T_{rot}(IS) = 715(13)$ K, and $\alpha_f = 0.31(3)$. For consistency with experiment, we also fit with T_{rot}(TD) fixed at 300 K, yielding similar values of $T_{rot}(IS) = 740(10)$ K, and $\alpha_f = 0.37(1)$. The fit and individual TD and IS components are plotted in Figure 4a to illustrate the accuracy with which the model reproduces the data. This two-temperature characterization shows that the majority of trajectories scatter through the IS channel with nearly one-third scattering through a TD channel with T_{rot}(TD) at nearly T_S. Integrated over all final scattering directions, these flux values appear somewhat colder and less accommodated than noted above for column integrated density measurements at $\theta_{scat} = 0°$. However, this is largely due to (i) differences in scattering angles and (ii) flux versus density considerations, as we shall see below.

The first step toward direct comparison between the MD simulations and experimental measurements involves parsing

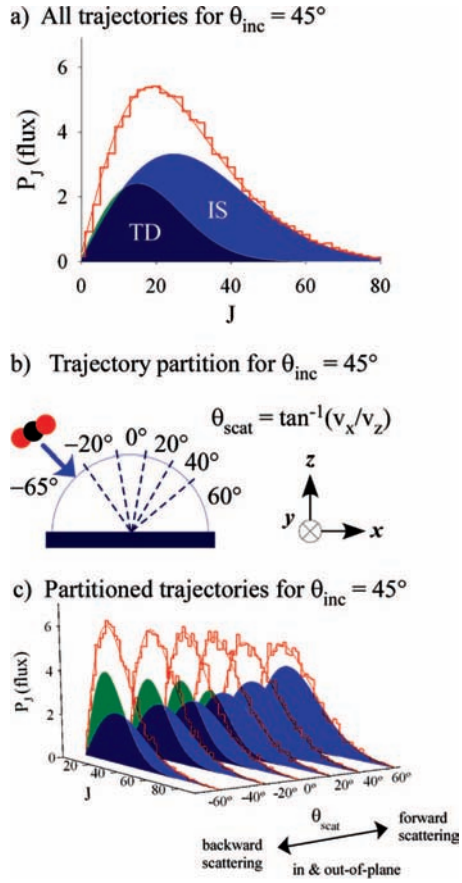

Figure 4. Sample rotational state populations for MD simulations where $\theta_{inc} = 45°$ and $E_{inc} = 10.6$ kcal/mol. (a) Probability distribution in percent for all trajectories is fit to a two-temperature model to extract TD and IS rotational temperatures and TD fraction (α_f). (b) To directly compare with experimental results, trajectories are parsed by final scattering angles defined in the illustration. (c) Probability distributions for each group of θ_{scat} trajectories are fit to the two-temperature model to characterize the scattering dynamics as a function of final angle.

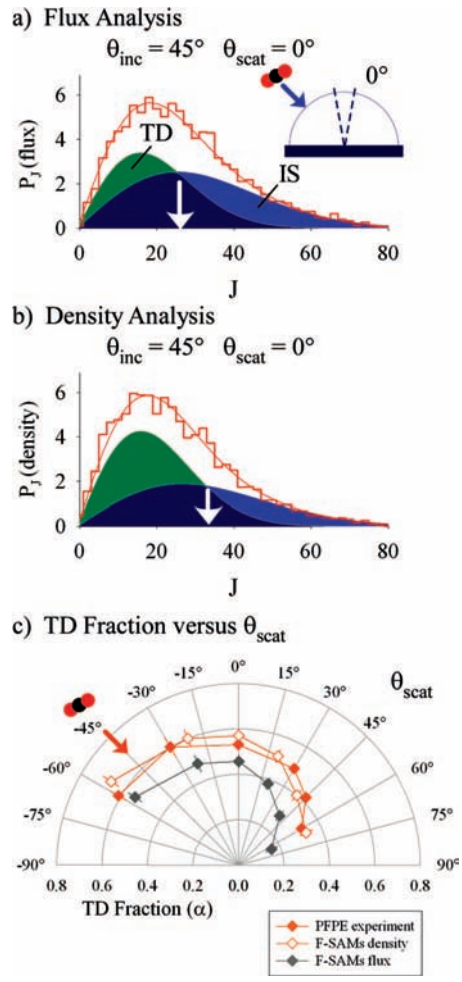

Figure 5. Accurate comparison with experiment involves a flux-to-density transformation. (a) Flux-based probability distribution for $\theta_{inc} = 45°$ and $\theta_{scat} = 0°$ illustrates a two-temperature fit where each trajectory within a given J-state is equally weighted. (b) Density-weighted P_J where the transformation between flux and density requires weighting each trajectory in a given bin by the transit time across a hypothetical laser beam to directly simulate the absorption event. (c) TD fraction for flux (α_f) and density (α_d) is plotted versus θ_{scat} for $\theta_{inc} = 45°$ to illustrate comparison between experiment and theory.

the trajectories by final scattering angle. The cartoon in Figure 4b shows an incoming CO_2 molecules that strikes the surface at $\theta_{inc} = 45°$. To best replicate the experimental probe geometry, the final angle is binned by $\theta_{scat} = \tan^{-1}(v_x/v_z)$), including all in-plane ($|v_y| \approx 0$) and out-of-plane trajectories ($v_y > 0$) within a given range of scattered velocity ratio. Partitioning the trajectories in this fashion is analogous to the column integrated densities from Section IIIA, for which in-plane and out-of-plane CO_2 scattering events are counted by integration over the Doppler profile. Trajectories are sorted into ≈ 6 bins from $\theta_{scat} = -90$ to $+90°$, from which rotational state distributions [P_J(flux)] are generated for each θ_{scat} group and plotted in Figure 4c. Individual P_J(flux) distributions are fit with eq 2 to characterize the two-temperature dynamics as a function of θ_{scat}, where, to be consistent with experimental studies, the TD temperature is fixed at 300 K. The overall fit and individual components plotted in Figure 4c reveal several trends worth noting. First, the final distributions for all θ_{scat} are well characterized by the two-temperature model, while the accommodation branching ratio (α_f) between the two channels shifts downward (i.e., toward IS) as θ_{scat} increases. This is expected based on a simple physical picture of TD flux desorbing in a cos(θ_{scat}) pattern; the increased IS contribution reflects a tendency for the CO_2 to scatter in the forward direction. Further analysis of the final angular and quantum state distributions as a function of θ_{inc} will be presented in Section IV.

As a second important consideration, the trajectories must be sorted by density before rigorous comparison between theory and experiment can be made. Experimental laser-based detection methods directly measure absorbances of the scattered CO_2, which by Beer's law is proportional to absolute density in a given quantum state. In contrast, MD simulations count individual trajectories that scatter from the surface and thereby determine molecular flux into a defined range of scattering angles. However, since final coordinates and momenta are known in the simulations, one can readily convert from flux to density based on the simple geometric considerations illustrated in Figure 2a. Specifically, the absorption probability of CO_2 is directly proportional to transit time across the probe laser;[62,63] we thus weight each trajectory by $v_\perp^{-1}$, where $v_\perp = (v_x^2 + v_z^2)^{1/2}$, to generate density-based rotational state distributions, P_J(density). One consequence is that slower molecules have a greater detection probability in an absorbance measurement than faster molecules. This is important because previous gas−liquid Dopplerimetry studies have already identified correlations in quantum state-dependent translational distributions for which higher rotational states tend to scatter with faster speeds.[16,19,20,22] From these observations, one would expect such a flux-to-

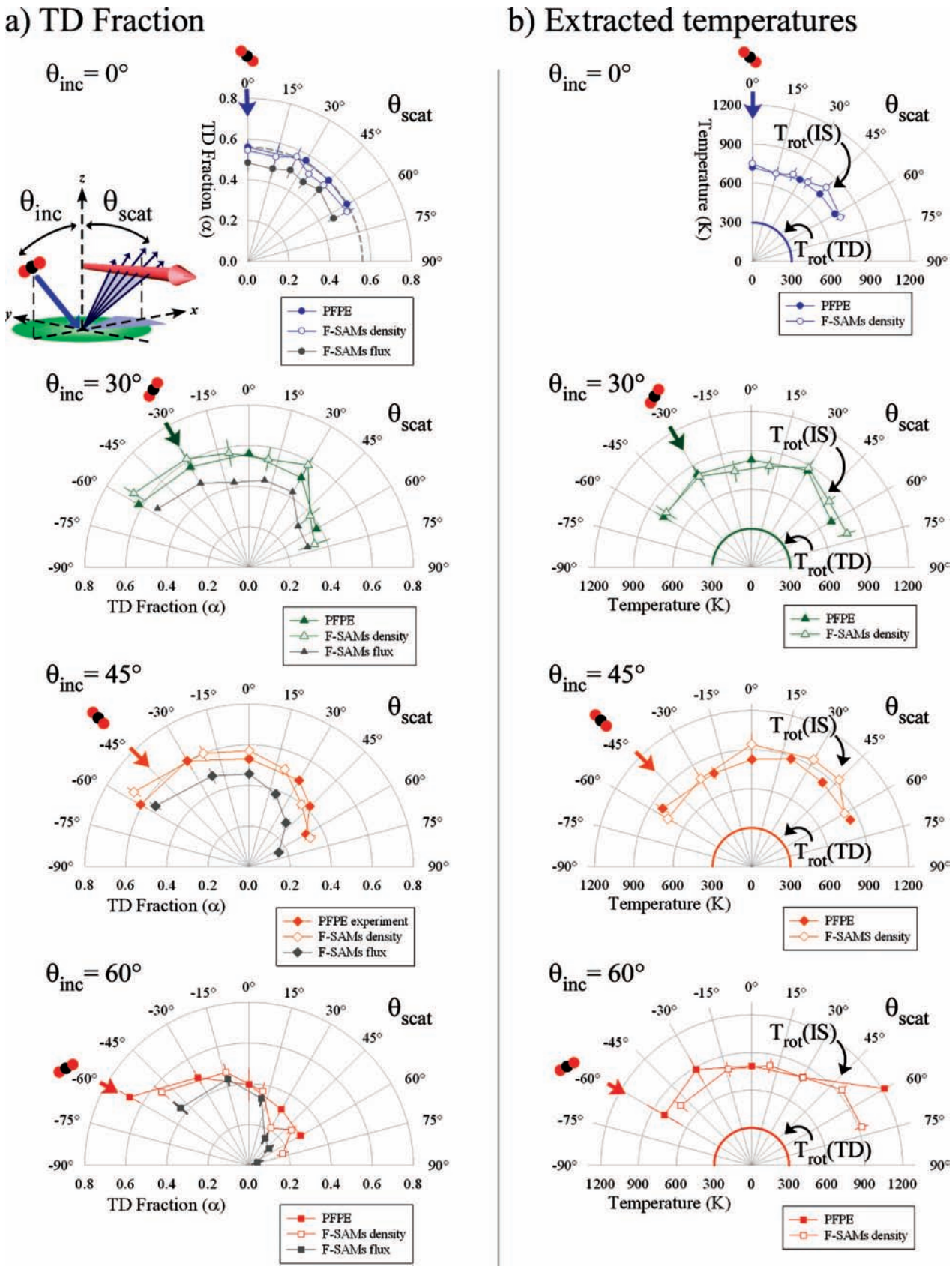

Figure 6. A direct comparison between experimental and theoretical results over all incident and final scattering angles. Values for (a) TD fraction and (b) extracted temperatures directly compare the experimental CO_2 + PFPE scattering with flux- and density-weighted probability distributions for CO_2 + F-SAM simulations.

density transformation to impact the comparison between experiment and MD simulations, specifically by overestimating the TD scattering fraction in a density-based measurement.

With the MD trajectory results now sorted by scattering angle and transformed from flux-to-density, we can quantitatively explore the differences in the two approaches with our two-

temperature model. The sample data in Figure 5a reflects the case for $\theta_{inc} = 45°$ and $\theta_{scat} = 0°$, in which the trajectories are equally weighted by flux and binned by final J-state. For comparison, the histogram in Figure 5b reflects the same group of trajectories, renormalized so that each trajectory is density weighted by $\nu_{\perp}^{-1}$. While the histograms appear qualitatively similar, a two-temperature fit to eq 2 reveals quantitative differences in the flux (α_f) versus density (α_d) trapping probabilities. Specifically, the TD fraction differs substantially ($\approx$ 25%), where $\alpha_f = 0.43(3)$ compared to $\alpha_d = 0.55(3)$. In contrast, the least-squares fitted rotational temperatures remain nearly the same for the two histograms, in which $T_{rot}(IS) = 750$ (30) K versus 820(40) K for flux versus density-weighted distributions, respectively. Fits of the data with a floated value of $T_{rot}(TD)$ converge to similar parameter values, where the temperature for the TD component is 298(32) K and 301(27) K for two respective analysis schemes. As mentioned above, the systematic disparity in TD fraction between flux- and density-based measurements is consistent with a correlation between final rotational, angular and translational distributions noted from earlier studies of CO_2 + PFPE. Such a flux-to-density transformation is clearly essential to the accuracy with which theoretical simulations can be meaningfully compared with experimental measurements as discussed below.

C. Comparison between Experiment and Theory. With angle-resolved and flux-to-density analysis schemes for the MD simulations, we now attempt rigorous comparison with our previously published experimental results. We first compare the TD fraction for $\theta_{inc} = 45°$ in Figure 5c, which illustrates α versus θ_{scat} for (i) PFPE liquid experiment results and (ii) F-SAM model simulations for both flux- and density-weighting schemes. In an independent set of tests, we have also fit each group of trajectories with the TD temperature both fixed and floated. While the qualitative nature of the two types of fits remains the same, slight deviations away from $T_{rot}(TD) \approx 300$ K are apparent in forward scattering directions where the relative fraction of TD to IS population decreases. Therefore, to provide a consistent comparison in each fit, the TD temperature is fixed at 300 K so that we systematically analyze the data from experiment and theory in the same manner. In general, the experimental TD fraction α has been shown to systematically decrease by over 2-fold as θ_{scat} increases from −60 to +60°, indicating that the CO_2 preferentially scatters in the forward direction. This same qualitative trend is reiterated theoretically in both the flux- and density-based TD fractions, but the density-weighted analysis for the F-SAM studies quantitatively reproduces the experimental values at each scattering angle.

As a next step, we quantitatively compare CO_2 scattering from PFPE and F-SAMs over the full range of incident angles (see Figure 6). For each θ_{inc}, scattered MD rotational state distributions are generated for both flux and density-weighting schemes. To be consistent with experimental analysis, distributions are again fit to eq 2 with the TD temperature fixed at 300 K. The resulting least-squares fitted $\alpha_{f/d}$ and $T_{rot}(IS)$ values are summarized in Table 2 and displayed graphically in Figure 6. We first examine the TD fraction as a function of final scattering angle in Figure 6a. The experimental results reveal several clear trends in α versus θ_{scat} as θ_{inc} shifts from normal to glancing incidence. First of all, at $\theta_{inc} = 0°$ the TD fraction remains nearly constant for $\theta_{scat} = 0$ to 60°, which, rather surprisingly at first, suggests that the TD and IS fractions scatter with nearly identical final angular distributions. Since the thermalized TD component is presumably quite well represented by a $\cos^n(\theta_{scat})$ distribution with $n \approx 1$, this would imply similarly highly diffuse scattering

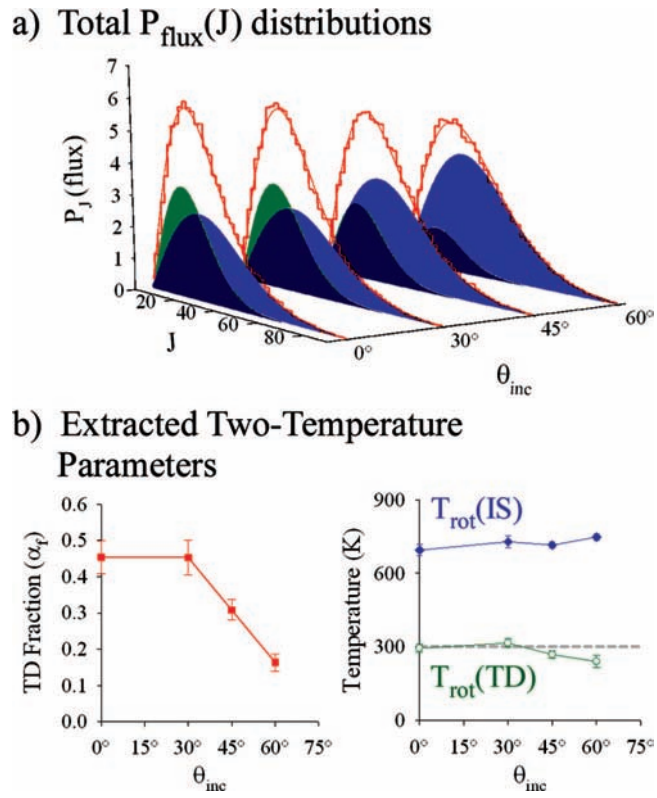

Figure 7. Two-channel dynamics for $\theta_{inc} = 0$, 30, 45, and 60°. (a) Probability distributions versus θ_{inc} for $E_{inc} = 10.6$ kcal/mol and $T_S = 300$ K. (b) Extracted TD fraction and temperatures reflect the probability of trapping decreases with incident angle.

even in the nominally impulsive scattering channel. Such behavior is indeed supported by previous angle dependent studies,[18,19] and likely reflects the rough nature of the liquid surface sampled by direct "head-on" collisions (i.e., $\theta_{inc} = 0°$). Note that while the transformation provides nearly quantitative agreement, the density-weighted trajectory analysis once again systematically overestimates the true sticking probability defined by the flux-based α_f.

As θ_{inc} increases, we observe that the TD fraction decreases rapidly from backward to forward scattering, with the most dramatic effects ($\approx$7-fold decrease between $\theta_{scat} = -60$ to 60°) observed at 60° incidence. In nearly every case, we see that the TD fraction for density-weighted rotational state distribution quantitatively matches the experimental result, while the flux-based distributions clearly indicate smaller absolute sticking probabilities. Similarly, the IS rotational temperatures are plotted as a function of incident and final scattering angle in Figure 6b. Consistent with our treatment of the experimental data, the TD rotational temperatures are fixed at T_S in each of the least-squares fits (as denoted by the solid lines) with the data presented only for a density-weighted analysis of the MD trajectories. In light of the considerable dynamic range of incident ($\theta_{inc} = 0$ to 60°) and final ($\theta_{scat} = -60$ to 60°) scattering angles sampled, the results illustrate a truly remarkable level of quantitative agreement between experiment and theory. This is perhaps even more noteworthy based on approximation of the liquid PFPE surface as a perfluorinated octanethiol model SAM.

IV. Analysis and Discussion

A. Dependence on Incident Angle. We first look to characterize trajectory dynamics as a function of incident scattering angle. To address this issue, normalized rotational

TABLE 2: Two-Temperature Boltzmann Analysis[a] of CO_2 + F-SAM Simulation[b]

			flux[c]		density[c]	
θ_{inc}	$<\theta_{scat}>$[b]	θ_{scat} range	α_f	T_{rot}(IS) (K)	α_d	T_{rot}(IS) (K)
0°	0°	0 to 10°	0.48(4)	720(40)	0.54(5)	750(50)
0°	15°	10 to 20°	0.47(5)	690(40)	0.53(6)	700(50)
0°	25°	20 to 30°	0.49(4)	740(40)	0.57(5)	740(60)
0°	35°	30 to 40°	0.47(4)	740(40)	0.52(5)	740(50)
0°	50°	40 to 50°	0.49(4)	790(50)	0.53(5)	790(60)
0°	75°	50 to 90°	0.47(3)	710(30)	0.54(3)	750(40)
30°	−55°	−90 to −40°	0.53(3)	690(30)	0.67(6)	770(90)
30°	−30°	−40 to −20°	0.48(4)	670(30)	0.61(6)	810(90)
30°	−10°	−20 to 0°	0.43(4)	670(30)	0.57(7)	750(80)
30°	10°	0 to 20°	0.44(3)	760(20)	0.54(6)	790(70)
30°	30°	20 to 40°	0.33(3)	780(30)	0.58(4)	880(70)
30°	50°	40 to 60°	0.32(4)	760(30)	0.39(6)	780(60)
30°	70°	60 to 90°	0.31(4)	780(40)	0.34(8)	780(70)
45°	−55°	−90 to −35°	0.54(4)	670(30)	0.67(4)	810(60)
45°	−20°	−35 to −10°	0.48(4)	710(40)	0.60(4)	770(50)
45°	0°	−10 to 10°	0.43(3)	750(30)	0.55(3)	820(40)
45°	20°	10 to 30°	0.38(3)	790(30)	0.51(3)	880(40)
45°	40°	30 to 50°	0.28(3)	800(20)	0.40(3)	840(40)
45°	65°	50 to 90°	0.16(3)	780(20)	0.33(3)	840(30)
60°	−50°	−90 to −30°	0.44(4)	670(30)	0.56(5)	740(70)
60°	−15°	−30 to 0°	0.43(3)	750(30)	0.47(4)	790(60)
60°	10°	0 to 20°	0.33(3)	780(30)	0.37(4)	810(60)
60°	30°	20 to 40°	0.15(3)	780(20)	0.21(3)	810(40)
60°	50°	40 to 60°	0.13(3)	850(20)	0.27(3)	940(50)
60°	70°	60 to 90°	0.04(3)	860(20)	0.17(3)	930(60)

[a] T_{rot}(TD) is fixed at T_S = 300 K in the nonlinear least-squares fit. [b] Configuration is illustrated in Figure 2b with $\theta_{scat} = \tan^{-1}(v_x/v_z)$. Average θ_{scat} is calculated for the trajectories that fall within the selected range of final angles. [c] Flux-based rotational state distributions equally weight each trajectory, whereas density-weighted probabilities are created through a flux-to-density transformation that is outlined in Section IIIB. [d] Numbers in parentheses represent the estimated error from a nonlinear least-squares fit.

TABLE 3: Two Temperature Boltzmann Analysis[a] of CO_2 + F-SAM Trajectories

θ_{inc}	trajectories	α_f	T_{rot}(IS) (K)	T_{rot}(TD) (K)
0°	26,502	0.45(5)[a]	695(23)	294(15)
		0.47(2)[b]	702(13)	300
30°	31,699	0.45(4)	729(25)	315(17)
		0.42(2)	711(12)	300
45°	32,115	0.31(3)	717(13)	268(15)
		0.37(1)	740(10)	300
60°	32,029	0.16(2)	748(12)	240(25)
		0.22(1)	771(10)	300

[a] Numbers in parentheses represent the estimated error from a nonlinear least-squares fit. [b] Fit values for fixed value of T_{rot}(TD) = T_S = 300 K.

state distributions, P_J(flux), summed over all final angles are generated and plotted in Figure 7a for each of the four values of θ_{inc}. Each histogram is then least-squares fit to eq 2, with T_{rot}(TD), T_{rot}(IS), and α_f now all floated in order to best characterize the scattered flux into the full 2π steradians. In the context of a simple collision model, one might expect a strong dependence of the TD branching fraction, α_f, on incident angle, as this angle can greatly impact the probability of being trapped on the liquid surface. Similar arguments could be made for the amount of incident energy converted from translation into rotation in impulsive scattering events, and thus suggesting that the IS temperature be a function of θ_{inc}. In contrast, the fate of molecules already relaxed and trapped on the surface should be insensitive to past history of the collision event; thus one expects $T_{TD} \approx T_S$, with essentially no dependence on incident angle.

Observations are in partial agreement with these predictions. First of all, α_f is indeed strongly sensitive to incident angle, exhibiting a nearly 3-fold drop-off with increasing angle of incidence (see Figure 7b, left). Interestingly, however, the negative slope of this effect (i.e., lower sticking efficiency at higher glancing angle) is not obvious, since accessing the TD channel nominally requires loss of the normal momentum component perpendicular to the surface. On the other hand, the TD rotational temperatures are approximately constant, as predicted, with T_{rot}(TD) $\approx T_S \approx$ 300 K, at least at low θ_{inc}. For the highest θ_{inc} values, however, the T_{rot}(TD) values appear to drop below T_S,[48] which brings into question the appropriate dynamical interpretation of a fully equilibrated, trapping desorption model. Reduced desorption temperatures have been observed in other systems as well,[64,65] where the microscopic picture involves either the dynamics of the last collision[64,65] or the energy/angular dependence of the sticking probability.[48] One might expect T_{rot}(TD) < T_S if rotation is strongly coupled to translation in the mechanism for adsorption and desorption. In this picture, CO_2 may desorb preferentially after rotational energy is transferred to translation normal to the surface. If the surface fails to replenish energy in CO_2 rotation, then the final J-state distribution will be colder than T_S. The fact that we see an anglular dependence to T_{rot}(TD) suggests this may not be the full physical picture. Instead, detailed balance and sticking probabilities may provide insight, where nonunity values of α_f at low E_{inc} may skew the TD temperature as a function of angle. Further studies of the two channel dynamics as a function of E_{inc} and θ_{inc} would provide evidence of such effects. In terms of the IS population, rotational temperatures appear to increase only by ≈8% from normal to 60° incidence, which largely reflects averaging a highly angle dependent rotational state distribution over all final angles. Indeed, least-squares fitted T_{rot}(IS) values from trajectories binned by final angle (Figure 6b) indicate that molecules scattered in the forward direction have much more energy in rotation compared to backward or

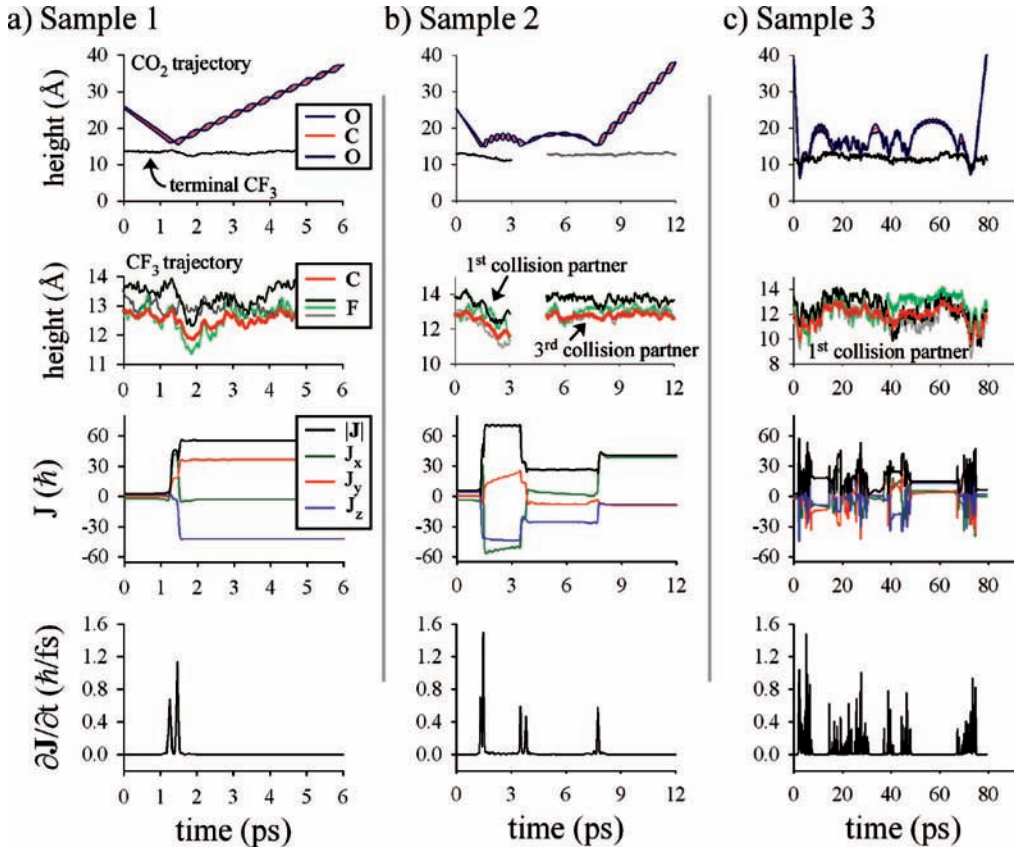

Figure 8. Sample time-dependent trajectories that show the z-heights (angstroms) of projectile and surface CF_3 atoms above the Au base layer, CO_2 angular momentum (J_x, J_y, J_z, and $|\mathbf{J}|$, in $\hbar$), and impulsive torques ($\hbar$/femtosecond) throughout the collisional interaction. Surface atom trajectories include the first terminal CF_3 group to be hit by the CO_2. Sample 2 also includes the time profile for the last CF_3 group hit before CO_2 scatters from the surface.

sideways scattered trajectories. This underscores the point that IS characterization with a single "temperature" is clearly only an approximate metric for describing the broad range of final scattering states. Indeed, we fully anticipate that more sophisticated distributions will clearly be necessary for representing nonequilibrium dynamics at the gas−liquid surface. Nevertheless, Figures 3−6 and Tables 2−3 suggest a perhaps surprising quantitative value in such an approximate two-temperature description with TD and IS channels reflecting (i) near equilibration versus (ii) multiple but finite interactions at the gas−liquid interface, respectively.

We return to the above trend of decreasing TD fraction with increasing θ_{inc} in Figure 7a. Such a phenomenon directly contrasts with results from gas-metal scattering systems such as Ar + Pt(111)[66,67] and NO + Ag(111)[68] in which the sticking probability generally *increases* with θ_{inc} due to the nature of energy transfer at the surface. A common motif in these gas-metal surface studies involves parsing the incident kinetic energy into "normal" and "parallel" components, where for a flat, frictionless surface, momentum can be transferred only along the normal direction. Once an incident molecule dissipates sufficient energy in this direction, it can no longer escape the surface potential and becomes trapped. Since the normal energy component scales as $E_{inc}\cos^2(\theta_{inc})$, glancing angles require less momentum transfer along the z-direction, which in turn might be expected to increase the trapping probability. In terms of liquid surfaces, this intuition appears to fail completely with indeed a strong trend in exactly the opposite direction.[26−28,33,38] One important difference is the much higher roughness and local corrugation at the gas−liquid versus gas-single crystal interface, which therefore favors conversion of incident kinetic energy into rotation and, importantly, translation away from the surface where the effects increase with θ_{inc}.

B. Scattering Angular Distributions. In addition to trends in the sticking probability, the final angular distributions also provide direct insight into nonequilibrium dynamics at the surface. Final scattering directions provide evidence on the number and diversity of these interactions, where, for example, single elastic collisions lead to more nearly specular scattering, while complete randomization of the incident direction results in a more $\cos(\theta_{scat})$ weighted flux distributions. MD simulations provide the ideal opportunity to investigate the underlying heterogeneity within an ensemble of trajectories. To help demonstrate these effects, we illustrate three distinctive pathways in Figure 8, that each involve a range of important interactions. In Figure 8a, the CO_2 strikes the surface in a single collision that transfers considerable energy from translation into rotation. The time profile of the projectile's height provides a qualitative sense of the collision, while important details are visible in the time dependence of angular momentum and torque ($\hbar$/femtosecond) along the x, y, and z-axes. To quantify this interaction, we plot the time dependence of J_x, J_y, J_z, $|\mathbf{J}|$, and torque (T), for which the magnitude is

$$|\mathrm{T}| = \frac{\partial|\mathbf{J}|}{\partial t} = \sqrt{\left(\frac{\partial J_x}{\partial t}\right)^2 + \left(\frac{\partial J_y}{\partial t}\right)^2 + \left(\frac{\partial J_z}{\partial t}\right)^2} \quad (3)$$

From the time profiles in Figure 8a, a more or less single direct collision torques the CO_2 along the y- and z-directions, while redirecting the center-of-mass away from the interface. In Figure 8b, we observe the exchange of energy between translation and

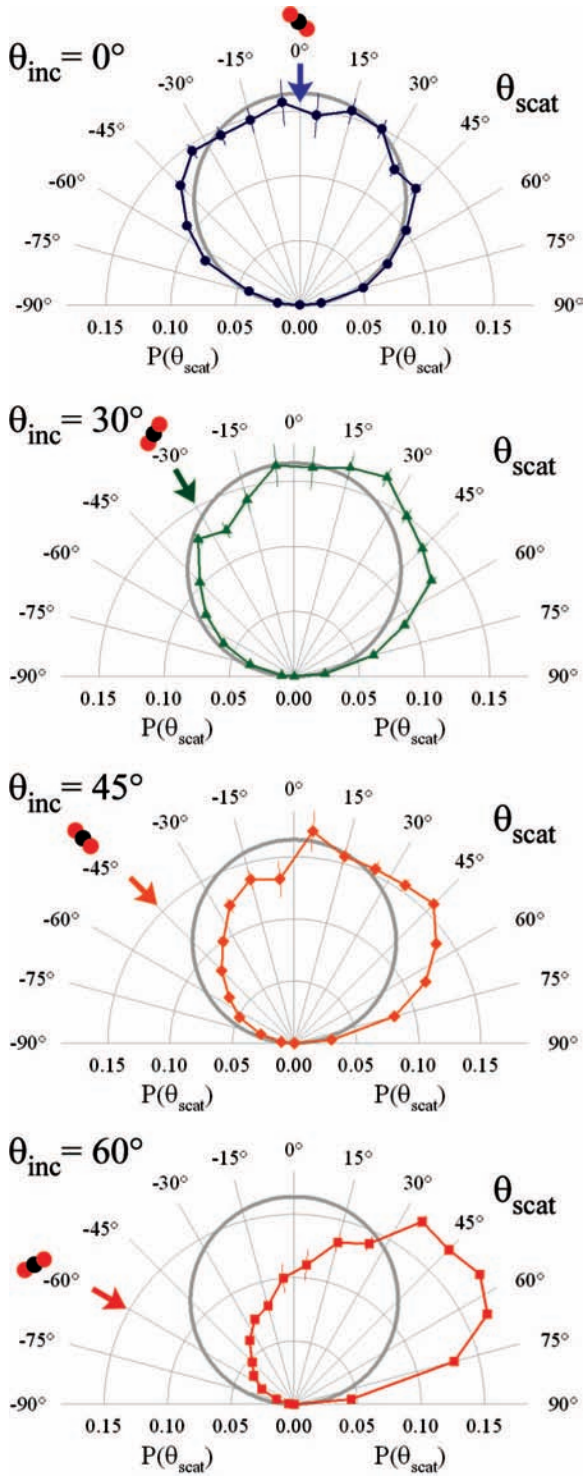

Figure 9. Final polar angular distributions for $\theta_{inc} = 0$ to 60°. Distributions are generated for in-plane scattering trajectories, which are defined to be within ±20° of forward scattering ($\varphi_{scat} = 0°$) or backward scattering ($\varphi_{scat} = 180°$). The gray line in each plot represents a cos(θ_{scat}) angular distribution.

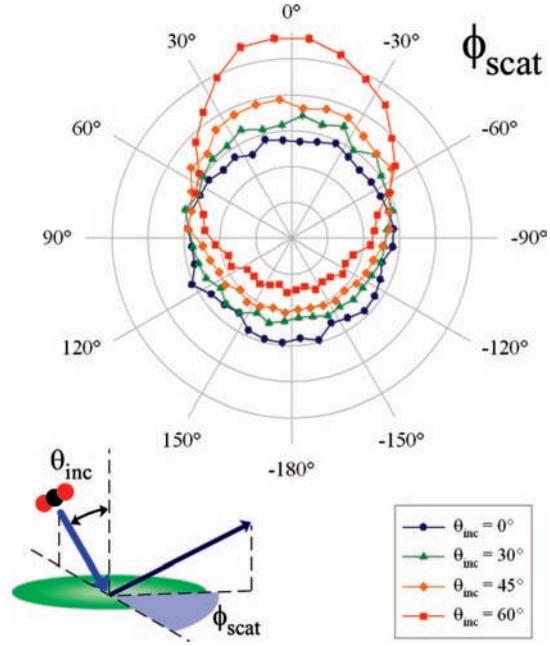

Figure 10. Final azimuthal angular distributions for $\theta_{inc} = 0$ to 60°.

rotation ("bouncing") through several surface interactions well isolated in time. These first two paths involve limited contact with an interaction that lasts ≈1−10 ps. By way of contrast, the trajectory in Figure 8c shows a trapped and partially solvated CO_2 that spends nearly 70 ps in close association with the gas−liquid interface, with torque continually redistributing angular momentum through a near continuum of collisional impacts. These trajectories provide three "motifs" for the energy, force, and time scales that define the interfacial interaction between a gas and liquid. Examination of the angular distributions offers additional vectorial insight into the nonequilibrium collision dynamics, which presumably is related to the success of a simple (albeit ad hoc) dual temperature description of the TD and IS components.

First, we examine the "in-plane" angular distributions for the full trajectory ensemble, defined to be within ±20° of forward scattering ($\varphi_{scat} = 0°$) or backward scattering ($\varphi_{scat} = 180°$) directions. Polar distributions for this subset of trajectories are shown for normal to glancing incident angles in Figure 9, where each plot also includes a cos(θ_{scat}) circle to represent the equilibrium angular distribution for thermally desorbing molecules. These in-plane polar distributions deviate from cos(θ_{scat}) for each incident angle, where the effects range from small at normal incidence to strongly shifted in the forward direction for $\theta_{inc} = 60°$. In our two-temperature picture, the small but finite deviations from cos(θ_{scat}) for $\theta_{inc} = 0°$ reflect the impulsive scattering channel, presumably with direct collisions on terminal $-CF_3$ groups favoring glancing ($\theta_{scat} \gg 0°$) versus back scattering ($\theta_{scat} \approx 0°$) trajectories. To help identify these trends more clearly, the final azimuthal distributions are plotted in Figure 10, which illustrate the evolution from spherically symmetric toward "lobular" forward scattering as θ_{inc} increases. Because these polar and azimuthal distributions include both TD and IS populations, a better functional form to characterize the scattering distribution would include (i) a cos(θ_{scat}) term for TD scattering and (ii) a shifted $\cos^n(\theta_{scat} - \theta')$ term for the IS pathway. Such a characterization parallels the distributions observed in angle-resolved $O(^3P)$ + squalane scattering studies.[26]

Detailed balance considerations prevent unambiguous classification of particular trajectories as purely "TD" or "IS". However, based on the two-temperature Boltzmann analysis for $\theta_{inc} = 60°$, the fraction of TD population that scatters with, say, $J > 40$ represents only ≈ 1/60 of the total number of trajectories. One way to selectively enhance the nonequilibrium collision dynamics, therefore, is to probe trajectories leading to high rotational states. The final polar scattering distribution is plotted in Figure 11a (red) for in-plane trajectories with $J > 40$. In addition to parsing by rotational states, we can also view angular

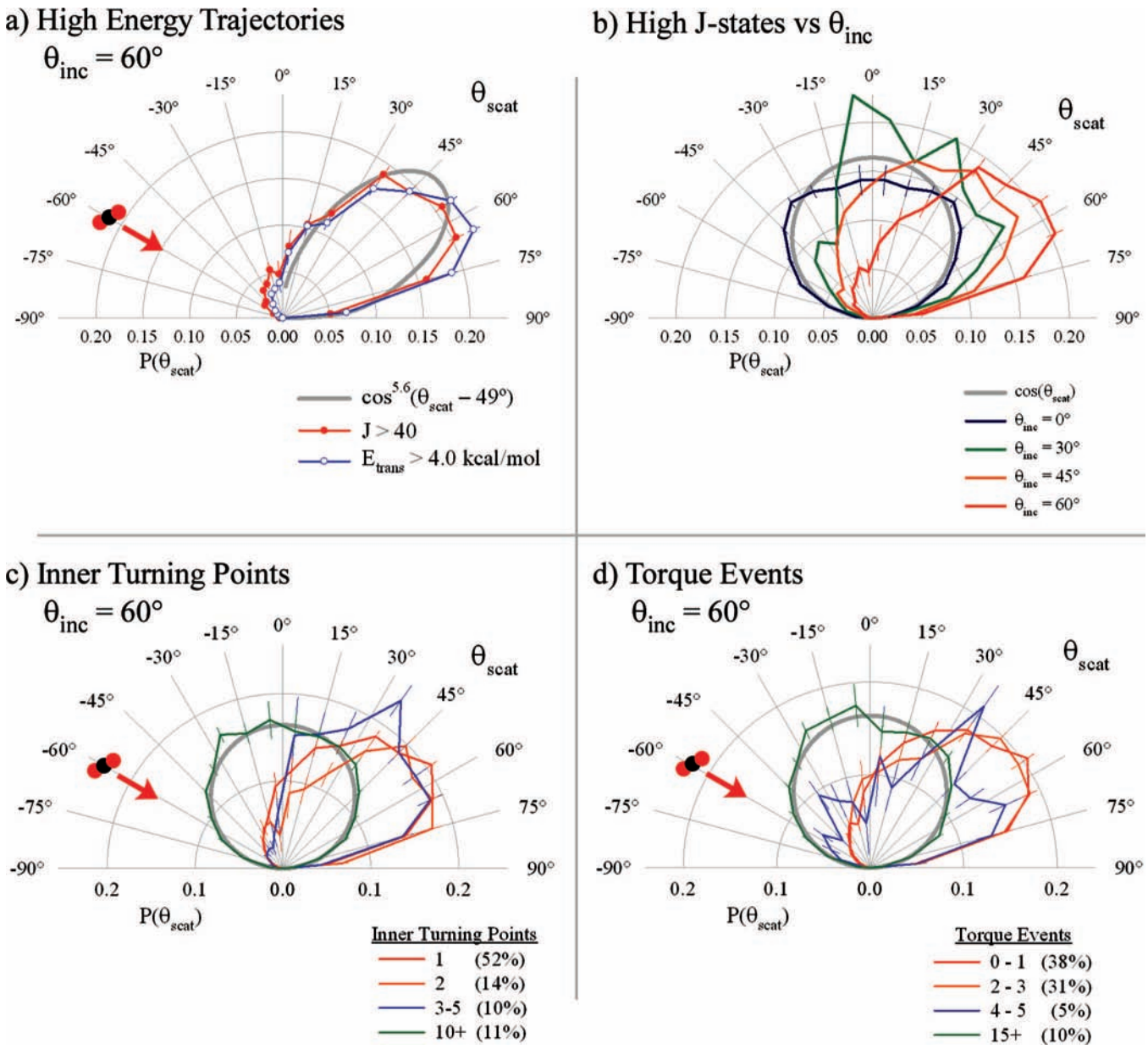

Figure 11. Angular in-plane scattering distributions for nonequilibrium trajectories. (a) High J-states ($J > 40$) and high translational energies ($E_{trans} > 4.0$ kcal/mol) for $\theta_{inc} = 60°$ selectively highlight the IS scattering component. (b) High J-state trajectories vary with incident angle, where final directions evolve into lobular forward scattering distributions. (c) Inner turning points (ITP) are defined by a change in sign of v_z for CO_2 throughout the trajectory. Final distributions are plotted against the number of ITP. (d) The nature of the trajectories are characterized by a change in the sign of J_x, J_y, or J_z, where the overall angular momentum changes by >0.03 ħ/femtosecond. The legends in panels c and d also list the fraction of centerline trajectories with the given ITP or torque event.

distributions of trajectories that scatter with $E_{trans} > 4.0$ kcal/mol, which would reflect a similarly favorable 60:1 ratio for IS versus TD components. As shown in blue in Figure 11a, the distribution of final scattering angles for these high kinetic energy trajectories are quite similar to the $J > 40$ distribution. For comparison, plotted alongside both of these curves in Figure 11a is a best fit of the $J > 40$ data to $\cos^n(\theta_{scat} - \theta')$, where $n = 5.6(1.2)$ and $\theta' = 49(2)°$. Such a functional form does not include back-scattered trajectories with $\theta_{scat} < \theta'$, but does permit comparison with inelastic angular distributions observed in $O(^3P)$ + squalane. Specifically, both systems are characterized by similar exponents ($n \approx 6$ vs 5.6), with mean values of θ' reflecting preferential scattering into a subspecular angle (42 vs 49°).[26] Indeed, each of the high J-state distributions plotted in Figure 11b as a function of θ_{inc} reveal broad scattering distributions that peak in the subspecular direction. While similar in shape, these lobular distributions differ from those measured for gas-metal systems, where the scattered flux peaks at superspecular angles.[68] Within a hard sphere collision model,[69] these superspecular angles reflect the transfer of momentum from the gas to a finite effective surface mass along the direction parallel to the surface normal. In a similar fashion, momentum must be transferred in the opposite direction for the intensity to peak at subspecular angles. Such a trend in gas−liquid scattering reflects the significance of local surface corrugations with CO_2 preferentially scattering from disordered surface sites. When viewed from the center of mass frame of the CO_2 and effective surface group, these final scattering angles require that the CO_2 preferentially scatters in the backward direction.[26] With increasing incident angle, these final distributions narrow substantially and tilt forward, which reflects the expected shift from TD to IS scattering.

We also consider two alternative criteria to highlight nonequilibrium scattering distributions, based on partitioning trajectories by the number of (i) inner turning points (ITP) or (ii) torque events involved in the interaction. An ITP for CO_2 consists of a v_z sign change from negative to positive during the trajectory; a torque event is triggered by a sign change in any J_x, J_y, or J_z component, when the magnitude of the torque is greater than $1\hbar$ over a 30 fs interval. Polar histograms are generated for each number of events and plotted in Figure 11c,d. The two $P(\theta_{scat})$ curves reveal similar trends in terms of the final shape of the distribution. Single ITP and torque events reveal lobular probabilities that peak at subspecular angles with the distributions broadening and shifting toward the surface normal with event number. However, after $\approx 10-15$ such interactions, the scattered flux has collapsed into an approximately $\cos(\theta_{scat})$ pattern, which indicates nearly complete loss of memory for the initial trajectory. As a check, we also investigated the effects of the torque event threshold by increasing the value to $10\hbar$ in 30 fs. The $P(\theta_{scat})$ curves with this threshold are indistinguishable from those in Figure 11d.

V. Summary and Conclusion

Experimental CO_2 + PFPE internal state and angular populations have been directly compared with the rotational state probability distributions from MD simulations of CO_2 + F-SAMs. Explicit details of the comparison involves parsing the trajectories by final scattering angles, and a simple, yet crucial, flux-to-density transformation that accurately corrects for the laser-based detection scheme. A two-temperature Boltzmann model is used to characterize the dynamics associated with energy transfer into the internal states of CO_2. We assume that the TD rotational temperature reaches thermal equilibrium with the surface, while the IS component is well-characterized by temperatures where $T_{rot}(IS) > T_S$. In addition, the sticking probabilities are determined as a function of θ_{inc} and θ_{scat} to provide a more detailed angular characterization of the two-channel dynamics.

On the basis of the quantitative agreement between experimental results and theoretical simulations, we exploit the MD trajectories to explore aspects of the final angular distributions. Final scattering distributions for the ensemble of trajectories evolve from nearly $\cos(\theta_{scat})$ for normal incidence to broad lobular distributions for glancing θ_{inc}. These $P(\theta_{scat})$ distributions show that incident molecules preferentially scatter in the forward direction that includes a large out-of-plane component. To help understand the nonequilibrium nature of these distributions, trajectories are sorted by high J-state, high kinetic energy, number of ITP, and number of torque events. Angular distributions for each metric reveal lobular patterns that peak in subspecular directions. A detailed fit for $\theta_{inc} = 60°$ shows $a \approx \cos^{5.6}(\theta_{scat} - 49°)$ pattern, in quite reasonable agreement with observations from $O(^3P)$ inelastic scattering studies of Minton and co-workers.

One powerful advantage of MD simulations is that they provide a time record of positions and momenta for each atom in the F-SAM surface. From these trajectories, we can therefore hope to elucidate relevant surface vibrational modes and time scales for the inelastic collision dynamics. Surface motion is illustrated in Figure 8 for the three sample trajectories, in which the time dependence is plotted for the z-position of the terminal $-CF_3$ atoms that are hit during the collision. These typical time traces reveal molecular motion on the surface that responds to the inelastic impact of the incoming CO_2, where the correlated recoil immediately follows the collision and persists for ≈ 1 ps. Such phenomena are closely related to the time scale for CO_2 rotation and translation at the surface, and therefore report on the mechanism by which these motions are coupled to stretches, bends, and collective movement of the surface atoms. Further quantitative analysis of the spectral density for surface vibrations, impact forces, and torques should prove extremely useful in clearly elucidating both key differences and similarities between gas−liquid and gas−solid interfacial scattering dynamics.

Acknowledgment. Primary support for this work is provided by the Air Force Office of Scientific Research with initial equipment and computer resource funding provided by the National Science Foundation. We would also like to thank Professors Bill Hase and Emilio Martínez-Núñez for their development of high quality CO_2−PFPE gas−liquid scattering potentials as well as many useful and stimulating discussions. Finally, we congratulate Professor George Schatz for his tireless efforts and numerous insightful contributions to the field of physical chemistry and chemical physics; we all owe him a great debt of gratitude.

References and Notes

(1) Nathanson, G. M. *Annu. Rev. Phys. Chem.* **2004**, *55*, 231.
(2) Nathanson, G. M.; Davidovits, P.; Worsnop, D. R.; Kolb, C. E. *J. Phys. Chem.* **1996**, *100*, 13007.
(3) Richmond, G. L. *Annu. Rev. Phys. Chem.* **2001**, *52*, 357.
(4) Giancarlo, L. C.; Flynn, G. W. *Annu. Rev. Phys. Chem.* **1998**, *49*, 297.
(5) Wodtke, A. M.; Matsiev, D.; Auerbach, D. J. *Prog. Surf. Sci.* **2008**, *83*, 167.
(6) Imbihl, R.; Ertl, G. *Chem. Rev.* **1995**, *95*, 697.
(7) Ertl, G. *Surf. Sci.* **1994**, *300*, 742.
(8) Somorjai, G. A.; Zaera, F. *J. Phys. Chem.* **1982**, *86*, 3070.
(9) Somorjai, G. A. *Surf. Sci.* **1979**, *89*, 496.
(10) Gross, A. *Surf. Sci. Rep.* **1998**, *32*, 291.
(11) Rettner, C. T.; Auerbach, D. J.; Tully, J. C.; Kleyn, A. W. *J. Phys. Chem.* **1996**, *100*, 13021.
(12) Wodtke, A. M.; Tully, J. C.; Auerbach, D. J. *Int. Rev. Phys. Chem.* **2004**, *23*, 513.
(13) Saecker, M. E.; Govoni, S. T.; Kowalski, D. V.; King, M. E.; Nathanson, G. M. *Science* **1991**, *252*, 1421.
(14) Saecker, M. E.; Nathanson, G. M. *J. Chem. Phys.* **1994**, *100*, 3999.
(15) Saecker, M. E.; Nathanson, G. M. *J. Chem. Phys.* **1993**, *99*, 7056.
(16) Perkins, B. G.; Nesbitt, D. J. *J. Phys. Chem. B* **2008**, *112*, 507.
(17) Perkins, B. G.; Nesbitt, D. J. *Proc. Natl. Acad. Sci. U.S.A.* **2008**, *105*, 12684.
(18) Perkins, B. G.; Nesbitt, D. J. *J. Phys. Chem. A* **2008**, *112*, 9324.
(19) Perkins, B. G.; Nesbitt, D. J. *J. Phys. Chem. A* **2007**, *111*, 7420.
(20) Perkins, B. G.; Nesbitt, D. J. *J. Phys. Chem. B* **2006**, *110*, 17126.
(21) Zolot, A. M.; Harper, W. W.; Perkins, B. G., Jr.; Dagdigian, P. J.; Nesbitt, D. J. *J. Chem. Phys.* **2006**, *125*, 021101.
(22) Perkins, B. G.; Haber, T.; Nesbitt, D. J. *J. Phys. Chem. B* **2005**, *109*, 16396.
(23) Kohler, S. P. K.; Allan, M.; Costen, M. L.; McKendrick, K. G. *J. Phys. Chem. B* **2006**, *110*, 2771.
(24) Allan, M.; Bagot, P. A. J.; Costen, M. L.; McKendrick, K. G. *J. Phys. Chem. C* **2007**, *111*, 14833.
(25) Bagot, P. A. J.; Waring, C.; Costen, M. L.; McKendrick, K. G. *J. Phys. Chem. C* **2008**, *112*, 10868.
(26) Minton, T. K.; Garton, D. J. Dynamics of Atomic-Oxygen-Induced Polymer Degradation in Low Earth Orbit In *Chemical Dynamics in Extreme Environments*; Dressler, R. A., Ed.; World Scientific Publishing Co.: Singapore, 2001; p 420.
(27) King, M. E.; Fiehrer, K. M.; Nathanson, G. M.; Minton, T. K. *J. Phys. Chem. A* **1997**, *101*, 6556.
(28) King, M. E.; Nathanson, G. M.; Hanninglee, M. A.; Minton, T. K. *Phys. Rev. Lett.* **1993**, *70*, 1026.
(29) Troya, D.; Schatz, G. C. *Int. Rev. Phys. Chem.* **2004**, *23*, 341.
(30) Troya, D.; Schatz, G. C. *J. Chem. Phys.* **2004**, *120*, 7696.
(31) Lipkin, N.; Gerber, R. B.; Moiseyev, N.; Nathanson, G. M. *J. Chem. Phys.* **1994**, *100*, 8408.
(32) Martinez-Nunez, E.; Rahaman, A.; Hase, W. L. *J. Phys. Chem. C* **2007**, *111*, 354.
(33) Yan, T. Y.; Hase, W. L. *Phys. Chem. Chem. Phys.* **2000**, *2*, 901.
(34) Kohler, S. P. K.; Reed, S. K.; Westacott, R. E.; McKendrick, K. G. *J. Phys. Chem. B* **2006**, *110*, 11717.

(35) McCullagh, M.; Prytkova, T.; Tonzani, S.; Winter, N. D.; Schatz, G. C. *J. Phys. Chem. B* **2008**, *112*, 10388.
(36) Nogueira, J. J.; Vasquez, S. A.; Mazyar, O.; Hase, W. L.; Perkins, B. G.; Nesbitt, D. J.; Martinez-Nunez, E. *J. Phys. Chem. A* [Online early access]. DOI: 10.1021/jp809756f. Published online: Jan. 20, 2009.
(37) Tasic, U.; Day, B. S.; Yan, T.; Morris, J. R.; Hase, W. L. *J. Phys. Chem. C* **2008**, *112*, 476.
(38) Gibson, K. D.; Isa, N.; Sibener, S. J. *J. Chem. Phys.* **2003**, *119*, 13083.
(39) Isa, N.; Gibson, K. D.; Yan, T.; Hase, W.; Sibener, S. J. *J. Chem. Phys.* **2004**, *120*, 2417.
(40) Yan, T.; Isa, N.; Gibson, K. D.; Sibener, S. J.; Hase, W. L. *J. Phys. Chem. A* **2003**, *107*, 10600.
(41) Alexander, W. A.; Day, B. S.; Moore, H. J.; Lee, T. R.; Morris, J. R.; Troya, D. *J. Chem. Phys.* **2008**, 128.
(42) Day, B. S.; Morris, J. R.; Alexander, W. A.; Troya, D. *J. Phys. Chem. A* **2006**, *110*, 1319.
(43) Scott Day, B.; Morris, J. R.; Troya, D. *J. Chem. Phys.* **2005**, *122*, 214712.
(44) Schatz, G. C.; Pederson, L. A.; Kuntz, P. J. *Faraday Discuss.* **1997**, *108*, 357.
(45) Ho, T. S.; Hollebeek, T.; Rabitz, H.; Harding, L. B.; Schatz, G. C. *J. Chem. Phys.* **1996**, *105*, 10472.
(46) Bowman, J. M.; Schatz, G. C. *Annu. Rev. Phys. Chem.* **1995**, *46*, 169.
(47) Kim, D.; Schatz, G. C. *J. Phys. Chem. A* **2007**, *111*, 5019.
(48) Rettner, C. T.; Schweizer, E. K.; Mullins, C. B. *J. Chem. Phys.* **1989**, *90*, 3800.
(49) Kenyon, A. J.; McCaffery, A. J.; Quintella, C. M.; Zidan, M. D. *Chem. Phys. Lett.* **1992**, *190*, 55.
(50) Quintella, C. M.; McCaffery, A. J.; Zidan, M. D. *Chem. Phys. Lett.* **1993**, *214*, 563.
(51) Zhang, J. M.; Garton, D. J.; Minton, T. K. *J. Chem. Phys.* **2002**, *117*, 6239.
(52) Minton, T. K.; Tagawa, M.; Nathanson, G. M. *J. Spacecr. Rockets* **2004**, *41*, 389.
(53) Garton, D. J.; Minton, T. K.; Alagia, M.; Balucani, N.; Casavecchia, P.; Volpi, G. G. *J. Chem. Phys.* **2000**, *112*, 5975.
(54) DuPont. Krytox Fluid Performance Sheets; 2003. Information is available at http://www2.dupont.com/Lubricants/en_US/products/Krytox/Krytox/Krytox.html.
(55) Day, B. S.; Shuler, S. F.; Ducre, A.; Morris, J. R. *J. Chem. Phys.* **2003**, *119*, 8084.
(56) Colorado, R.; Lee, T. R. *J. Phys. Org. Chem.* **2000**, *13*, 796.
(57) The notation (ν_1 ν_2 ^{l} ν_3) characterizes the vibrational state of CO_2; the quantum numbers ν_1, $\nu_.$, and ν_3 describe the symmetric stretch, bend, and antisymmetric stretch, and l is the vibrational angular momentum quantum number.
(58) Borodin, O.; Smith, G. D.; Bedrov, D. *J. Phys. Chem. B* **2002**, *106*, 9912.
(59) Alves, C. A.; Porter, M. D. *Langmuir* **1993**, *9*, 3507.
(60) Gang-yu, L.; Paul, F.; Christopher, E. D. C.; Ogletree, D. F.; Peter, E.; Miquel, S. *J. Chem. Phys.* **1994**, *101*, 4301.
(61) Hase, W. L. VENUS05; 2005. VENUS05 is an enhanced version of VENUS9L, which is available on the website cdssim.chem.Hu.edu.
(62) Comsa, G.; David, R. *Surf. Sci. Rep.* **1985**, *5*, 145.
(63) Sitz, G. O.; Kummel, A. C.; Zare, R. N. *J. Chem. Phys.* **1988**, *89*, 2558.
(64) Tully, J. C. *Surf. Sci.* **1981**, *111*, 461.
(65) Muhlhausen, C. W.; Williams, L. R.; Tully, J. C. *J. Chem. Phys.* **1985**, *83*, 2594.
(66) Mullins, C. B.; Rettner, C. T.; Auerbach, D. J.; Weinberg, W. H. *Chem. Phys. Lett.* **1989**, *163*, 111.
(67) Rettner, C. T.; Mullins, C. B.; Bethune, D. S.; Auerbach, D. J.; Schweizer, E. K.; Weinberg, W. H. *J. Vac. Sci. Technol., A* **1990**, *8*, 2699.
(68) Rettner, C. T.; Kimman, J.; Auerbach, D. J. *J. Chem. Phys.* **1991**, *94*, 734.
(69) Harris, J. Mechanical Energy Transfer in Particle-Surface Collisions In *Dynamics of Gas-Surface Interactions*; Rettner, C. T., Ashfold, M. N. R., Eds.; The Royal Society of Chemistry: Cambridge, 1991.

JP811322Y